The Astrophysical Journal, 860:160 (9pp), 2018 June 20 https://doi.org/10.3847/1538-4357/aac5f2

A Study of Electron Forbush Decreases with a 3D SDE Numerical Model

Xi Luo[1,2], Marius S. Potgieter[2], Ming Zhang[3], and Xueshang Feng[1]
[1] SIGMA Weather Group, State Key Laboratory of Space Weather, National Space Science Center, Chinese Academy of Sciences, Beijing 100190, People's Republic of China
[2] Centre for Space Research, North-West University, Potchefstroom 2520, South Africa
[3] Department of Physics and Space Sciences, Florida Institute of Technology, 150 West University Boulevard, Melbourne, FL 32901, USA
Received 2018 April 16; revised 2018 May 13; accepted 2018 May 14; published 2018 June 25

Abstract

Because of the precise measurements of the cosmic ray electron flux by the PAMELA and AMS02, Electron Forbush decreases (Fds) have recently been observed for the first time. This serves as motivation to perform a numerical study of electron Forbush decreases with an advanced time-dependent, three-dimensional (3D) stochastic differential equation model, developed earlier to study proton Fds. The model includes a realistic interstellar electron spectrum reconstructed from *Voyager* observations, and diffusion and drift coefficients to reproduce the modulated spectrum observed by PAMELA in 2009. On the basis of this numerical model, electron Fd profiles for a range of rigidities are simulated. In addition, a systematic comparison between electron and proton Fds during different solar polarity epochs is performed. This approach gives insight into the rigidity dependence of the heliospheric diffusion coefficients and of drift effects over two magnetic field polarity cycles. We find that during an $A > 0$ epoch, the recovery time of a 1 GV proton Fd is remarkably shorter than the 1 GV electrons, whereas the electron Fd display a faster recovery during an $A < 0$ epoch. This model clear predicts a charge-sign dependent effect in the recovery time of Fds but less so for their magnitude.

Key words: cosmic rays – Sun: activity – Sun: heliosphere

1. Introduction

Forbush decreases (Fds) are transient variations of a relatively short duration of cosmic ray (CR) intensity observed in the heliosphere. These phenomena, associated with solar activity, have been widely studied since their discovery 80 years ago (Forbush 1937). Utilizing the first neutron monitor type CR detector, a geographic latitude survey was carried out by Simpson (1953), who found that the CR intensity varied at all geomagnetic latitudes during a Forbush decrease event; Meyer & Simpson (1955) concluded that the origin for Fds is not terrestrial, but interplanetary. Later, Morrison (1956) and Meyer & Simpson (1957) proposed that the interplanetary turbulent magnetic fields within outward-propagating solar plasma clouds create these Fds.

Based on different space-borne instruments, additional delicate analyses have illustrated that it is the turbulent sheath region behind the preceding interplanetary shock that causes the CR intensity decrease during an Fd event (Zhang & Burlaga 1988). This general "reduced diffusion" mechanism has been successfully adapted in the numerical models to simulate Fds (Kadokura & Nishida 1986; le Roux & Potgieter 1991; Luo et al. 2017). It should be noted that there may be another CR intensity decreases associated with the solar ejecta. As a result, some Fds are characterized as "two-step" intensity decreases (Cane 2000). In this study, we focus on the main phase of a Fd, which is caused by the turbulent sheath region, with an effective localized reduction in all the diffusion coefficients.

Kadokura & Nishida (1986) and le Roux & Potgieter (1991) used a finite difference numerical scheme to solve the 2D transport equation for CRs. Various solar modulation effects on Fds, such as the change in the solar magnetic field polarity and the heliospheric current sheet (HCS) tilt angle, have been illustrated. More recently, Luo et al. (2017) utilized a Stochastic Differential Equation (SDE) numerical method to develop a classical proton Fd model by solving the full time-dependent, 3D transport equation. Correspondingly, this model revealed how the different diffusion components and the HCS's rotational motion affect the CR transport process and the features of Fds. As far as we know, all numerical studies of Fds are still limited to CR protons. Fortunately, as precise measurements of the lower-energy part of the CR electron spectrum from near-Earth satellites become possible, electron Fds have been recorded for the first time by the PAMELA mission (Munini et al. 2018). The AMS02 mission is capable of more precise measurements. Under such circumstances, we are motivated to develop a numerical model for studying electron Fds.

Our electron Fd model is based on the SDE-based 3D modulation model described in detail by Luo et al. (2017). For this approach, a propagating diffusion barrier is incorporated into the model, so that a Fd profile can be numerically simulated throughout the heliosphere. Various modulation parameters, such as the elements of the diffusion coefficients tensor, were validated by reproducing the PAMELA electron spectrum for solar minimum condition during 2009. Validation for proton modulation was done previously by Luo et al. (2017). Fd profiles are computed with the same rigidity for electrons and protons, and a wide range of rigidities are covered, which provides insight into the rigidity dependence of the main diffusion coefficients. The effects of particle drift on the magnitude of Fds and their recovery phase is revealed, and predictions are made concerning the effects of particle drifts.

The paper is organized as follows. A description of the transport process and the numerical model for electron Fds is given in Section 2, together with the assumed diffusion coefficients and the local interstellar spectra for electrons and protons; the simulation results are shown in Section 3, and Section 4 is devoted to discussions and conclusions.

2. Numerical Model

In this section, the numerical electron and proton Fd model is briefly described. We first introduce the numerical method on

solving the CR transport equation; second, the heliospheric magnetic field, the wavy HCS and the propagating diffusion barrier are described; third, the diffusion coefficients and drift coefficient are given; and finally, we provide the electron and proton local interstellar spectra.

2.1. Time-dependent Numerical Transport Model

Following Parker's argument (Parker 1965), galactic CRs encounter the solar wind and irregularities in the interplanetary magnetic field (IMF) when entering the heliosphere. These irregularities, which have the comparable size with the Lamour radius for hundreds of MeV CR particles, scatter these CRs, so that galactic CR propagation in the heliosphere is of a diffusion nature. Thus, we adapt the random walk of Brownian particles to deal with this physical process.

Parker (1965) derived the following equation for CR propagation in the heliosphere:

$$\frac{\partial f}{\partial t} = -(\boldsymbol{V}_{\rm sw} + \langle \boldsymbol{v}_d \rangle) \cdot \nabla f + \nabla \cdot (K^s \cdot \nabla f) + \frac{1}{3}(\nabla \cdot \boldsymbol{V}_{\rm sw}) \frac{\partial f}{\partial \ln p}. \quad (1)$$

Here, $f(\boldsymbol{r}, p, t)$ is the distribution function or the phase-space density as a function of spatial position, $\boldsymbol{r}$, momentum, p, and time, t; $\boldsymbol{V}_{\rm sw}$ is the solar wind velocity. The rigidity P is related to momentum by $P = pc_{\rm light}/q$, with $c_{\rm light}$ the velocity of light, and q the charge of the CRs. The differential intensity is related to the distribution function by $j \propto p^2 f$; $\langle \boldsymbol{v}_d \rangle$ is the pitch-angle averaged drift velocity, over the near-isotropic particle distribution, which is given by Jokipii et al. (1977):

$$\langle \boldsymbol{v}_d \rangle = \nabla \times \kappa_d \hat{e}_B. \quad (2)$$

Here, K^s is the diffusion tensor, which contains a diffusion coefficient parallel to the local magnetic field ($\kappa_\parallel$), and two diffusion coefficients perpendicular to the local magnetic field ($\kappa_\perp$): one in the heliospheric radial direction and one applicable to the polar directions; κ_d is the drift coefficient, and $\hat{e}_B$ is unit vector in the direction of the magnetic field.

2.1.1. The SDE Method

Zhang (1999) realized the stochastic nature of the individual CR particles as they propagate in the heliosphere, and adapted a set of SDEs to describe CR particle transport. In fact, the Ito formula can be used to change the transport equation given above to the following set of SDEs:

$$d\boldsymbol{X} = (\nabla \cdot K^{(s)} - \boldsymbol{V}_{\rm sw} - \langle \boldsymbol{v}_d \rangle) ds + \sum_\sigma \boldsymbol{\alpha}_\sigma dW_\sigma(s) \ ,$$

$$dP = \frac{1}{3} P(\nabla \cdot V) ds. \quad (3)$$

Here, W_σ is a Wiener process, which contains the Markov feature. Therefore, each increment $dW_\sigma(s)$ is independent of each other, and this set of SDEs can be integrated with the Euler–Maruyama numerical scheme. Correspondingly, the trajectories of pseudo particles in phase space are obtained by integration. The details of this numerical method were described in earlier publications, e.g., Zhang (1999), Kopp et al. (2012), Luo et al. (2011), and Qin et al. (2006). The SDE method is intrinsically time dependent, thus the time-dependent CR problem can be handled with unconditional stability (Luo et al. 2017). It is an ideal numerical tool to deal with the challenges of the numerical modeling of time-dependent CR phenomena such as Fds, which is extremely difficult with finite difference numerical methods in 3D space (that is, five numerical dimensions).

2.1.2. The Heliospheric Magnetic Field and Current Sheet

Similar to our previous work on proton Fds (Luo et al. 2017), Parker's IMF model is utilized:

$$\boldsymbol{B}(r, \theta) = \frac{A}{r^2}\left(\hat{e_r} - \frac{r\Omega \sin\theta}{V_{\rm sw}} \hat{e_\phi}\right)[1 - 2H(\theta - \theta_{\rm cs})]. \quad (4)$$

Here, r is the heliocentric radial distance (typically in au) from the Sun, Ω is the solar angular speed, and $V_{\rm sw}$ is the solar wind speed; A is a constant which indicates the magnetic field polarity (two drift cycles with $A > 0$ and $A < 0$) and determines the magnitude of the IMF; see Luo et al. (2017) for a more detailed description of the solar wind and IMF model.

Because the IMF is frozen into the outward-propagating solar wind plasma, a wavy HCS is formed because of the extension of the IMF sector structure with the rotation of the Sun; see Jokipii & Barry (1981) and Kóta & Jokipii (1983). In our numerical model, the HCS surface location (r, $\theta_{\rm cs}$,ϕ) is modeled through the following expression:

$$\cot(\theta_{\rm cs}) = -\tan(\alpha)\sin(\phi^*), \quad (5)$$

where α is the tilt angle of the HCS, $\phi^* = \phi + \frac{r\Omega}{V_{\rm sw}}$. To deal with the singular current sheet velocity, a square wave function, $\frac{r}{4R_g}$, replaces the δ function and the locally flat current sheet assumption is used in our numerical model, although the HCS is globally not flat (Luo et al. 2013, 2017). A forth-order RungeKutta method is implemented to integrate the HCS drift motion in the SDE numerical model. Utilizing this integration method avoids the problem of the pseudo particles possibly crossing the HCS. Correspondingly, our numerical model replicates the well-known drift pattern. Positive charged particles drift inward, mainly along the HCS during negative solar magnetic polarity epoch, while negative charged particles drift outward during negative solar magnetic polarity epoch (Jokipii & Barry 1981; Potgieter & Moraal 1985).

2.2. Diffusion Coefficients, Drifts, and Diffusion Barrier

Generally, the parallel diffusion coefficient $\kappa_\parallel$ is expressed as a function of space and rigidity:

$$\kappa_\parallel = (\kappa_\parallel)_0 \beta f_1(\boldsymbol{r}) f_2(P) \ . \quad (6)$$

The task at hand is to choose appropriate forms for the rigidity dependence $f_2(P)$ and spatial dependence $f_1(\boldsymbol{r})$ throughout the heliosphere.

The rigidity dependence of the diffusion coefficients have been investigated theoretically and as such not settled. However, it has been demonstrated that in general the rigidity dependence varies over rigidity range applicable to CR modulation (Bieber et al. 1994; Potgieter 1996; Teufel & Schlickeiser 2003; Zhao et al. 2014). In this study, following the work of Potgieter et al. (2015) and Vos & Potgieter (2015), who numerically reproduced both electron and proton spectra

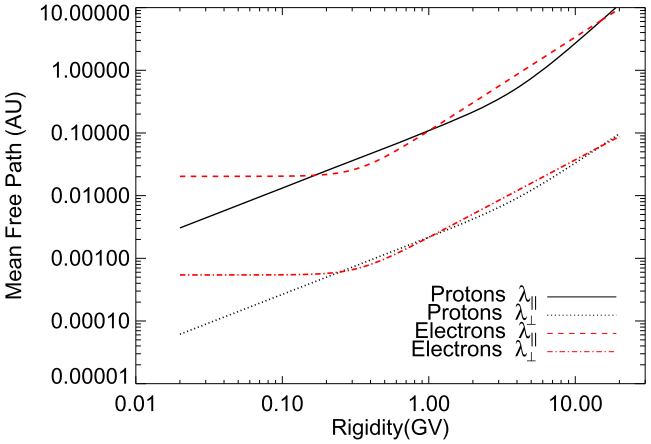

Figure 1. Comparison of MFPs at Earth for electrons and protons as a function of rigidity.

from PAMELA, an empirical approach is adapted assuming the following two-power-law form:

$$f_2(P) = \left(\frac{P}{P_0}\right)^a \left[\frac{\left(\frac{P}{P_0}\right)^c + \left(\frac{P_k}{P_0}\right)^c}{1 + \left(\frac{P_k}{P_0}\right)^c}\right]^{b/c}. \quad (7)$$

Here, $P_0 = 1$ GV. The parameters a and b determine the two power indices, P_k determines the rigidity where the power index varies, and c controls the smoothness of the variation of the power index with decreasing rigidity.

Following the work of e.g., Zhang (1999), Luo et al. (2017), Vos & Potgieter (2015), and Potgieter et al. (2015), the spatial part $f_1(r)$ is simply assumed to be inversely proportional to the IMF magnitude B, with B_0 in nT.

$$f_1(r) = \frac{B_0}{B}. \quad (8)$$

As for the two perpendicular diffusion coefficients, They scale according to the parallel diffusion coefficient with a constant ratio, typically with a value of 0.02:

$$\kappa_{\perp_r} = \kappa_{\perp_\theta} = (\kappa_{\perp_0})\kappa_{||}. \quad (9)$$

It should be noted that both the electron and proton diffusion coefficients have the same spatial dependence but because the parameters a, b, c, P_k differ, it results in different rigidity dependence, again following the approach of Potgieter et al. (2015) and Vos & Potgieter (2015).

Figure 1 illustrates how the Mean Free Path (MFP), $\lambda = 3\kappa/\beta c_{\rm light}$, varies with rigidity P for electrons and protons in our simulation model; β is the ratio of particle speed to the speed of light, c_l. Both proton (black curve) and electron (red curve) MFPs exhibit a two-stage power-law shape. In the rigidity range below 0.2 GV, the electron MFP is much larger than proton MFP and remains nearly unchanged in this range. The difference causes different behavior for electrons and protons in the simulated Fd profiles at these lower rigidities. As for the rigidity range $P > 1$ GV, both electron and proton MFPs vary similarly. This will be shown in the following section.

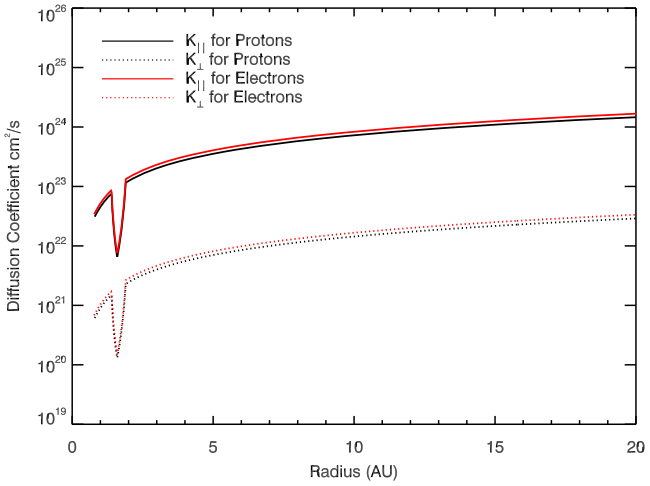

Figure 2. Diffusion coefficient values for electrons and protons at 1 GV, as a function of the heliocentric radial distance up to 20 au. Inside the diffusion barrier, the diffusion coefficients are reduced as illustrated.

As in our proton Fd model, the drift coefficient is based on the weak scattering approach, which gives

$$\kappa_d = (\kappa_d)_0 \frac{\beta P}{3B}; (\kappa_d)_0 = [0, 1]. \quad (10)$$

When $(\kappa_d)_0 = 1$, maximum drifts are assumed, and no drifts when $(\kappa_d)_0 = 0$; see e.g., Potgieter (2014b) and Ngobeni & Potgieter (2015). A 3D propagating diffusion barrier is constructed with the analytical form

$$\kappa'_{||,\perp,d} = \frac{\kappa_{||,\perp,d}}{[1 + h(\theta) f_k(r) g(\phi)]}, \quad (11)$$

where κ' is the respective diffusion and drift coefficients inside the diffusion barrier; and $h(\theta)$, $f_k(r)$, and $g(\phi)$ are the geometry characteristic functions of the diffusion barrier in terms of radial distance, polar, and azimuthal angles, respectively, with the following relationships:

$$h(\theta) = e^{-\left(\frac{\theta - \pi/2}{\theta_{\rm br}}\right)^{10}}, \quad (12)$$

$$g(\phi) = e^{-\left(\frac{\phi}{\phi_{\rm br}}\right)^{10}}. \quad (13)$$

Here, $\theta_{\rm br}$ and $\phi_{\rm br}$ are the maximum extent of this diffusion barrier along the $\hat{e_\theta}$ and $\hat{e_\phi}$ directions. In our simulation work, $\theta_{\rm br} = \frac{\pi}{4}$, $\phi_{\rm br} = \frac{5\pi}{6}$. And $f_k(r)$ is given by

$$f_k(r) = \begin{cases} 1 - \dfrac{r - r_{\rm cen}}{r_a} & \text{if } r_{\rm cen} < r < r_{\rm sh} \\ \dfrac{r - r_{\rm end}}{r_b} & \text{if } r_{\rm end} < r \leqslant r_{\rm cen} \\ 0 & \text{if } r \leqslant r_{\rm end}, r \geqq r_{\rm sh}. \end{cases} \quad (14)$$

The diffusion barrier's front location is $r_{\rm sh}$, and its end is at $r_{\rm end}$. $r_{\rm cen}$ is the location where the maximum reduced diffusion happened. $r_a = r_{\rm sh} - r_{\rm cen}$ is the width of the barrier's leading path, while $r_b = r_{\rm cen} - r_{\rm end}$ is the trailing path's width. Thus, the diffusion and drift processes are reduced inside this barrier (disturbance), which propagates outward with the solar wind speed (Figure 2); see Luo et al. (2017) for an elaborate discussion and how these assumptions play a role in simulating the features of a Fd.

2.3. Electron Local Interstellar Spectrum (LIS)

Solar modulation studies require that a LIS be specified for each CR species at the outer boundary of the heliosphere, typically assumed to be the heliopause (HP) (the outer boundary is a sphere with radius of 123 au in this numerical model). Different forms have been adapted over the years, see e.g., Jokipii et al. (1977), Potgieter & Moraal (1985), Zhang (1999), and Potgieter & Nndanganeni (2013). When *Voyager 1* crossed the HP at 121 au (Gurnett et al. 2013; Webber & McDonald 2015), direct measurements of the lower-energy end of the LIS became available, given that there seems nearly no modulation beyond the HP (Zhang et al. 2015; Luo et al. 2016). Together with the higher-energy side of the CR spectra measured recently by PAMELA and AMS02, the LIS for electrons and protons can be fully parameterized with improved accuracy, see e.g., Bisschoff & Potgieter (2014, 2016), Corti et al. (2016), Herbst et al. (2017), and the discussion on new LIS's by Potgieter (2014a).

For our work, the following LIS's are utilized, as they have already been successfully used to reproduce the PAMELA spectra (Adriani et al. 2013, 2015) during the solar minimum cycle 23/24, particularly for the period 2006–2009 (Potgieter et al. 2015; Vos & Potgieter 2015), and also for protons for the period 2010–2014 (Martucci et al. 2018).

For electrons:

$$j_{\rm LIS} = 0.21\frac{E^{-1.35}}{\beta^2}\left[\frac{E^{1.65}+0.6920}{1.6920}\right]^{-1.1515} + j_{\rm bump}, \quad (15)$$

with

$$j_{\rm bump} = 1.73\exp[4.19 - 5.40\log(E) - 8.9(E^{-0.64})]. \quad (16)$$

For protons:

$$j_{\rm LIS} = 2.70\frac{E^{1.12}}{\beta^2}\left(\frac{E+0.67}{1.67}\right)^{-3.93}, \quad (17)$$

as differential intensity in units of particles $\rm m^{-2}\,s^{-1}\,sr^{-1}\,MeV^{-1}$, but with E the kinetic energy in GeV, and β again the ratio of particle speed to the speed of light.

The electron LIS is displayed in Figure 3, as well as the computed electron spectrum at the Earth and compared to electron spectrum from PAMELA in 2009 (Adriani et al. 2015). See Vos & Potgieter (2015) for the proton LIS.

3. Simulation Results

In this section, several simulation results according to different cases are illustrated, together with relevant discussions. To validate our electron Fd model and fine-tuning the various modulation parameters, the model is applied first to reproduce the PAMELA electron spectrum measured in 2009 (Adriani et al. 2015), which is a six months average from 2009 July to 2009 December. As mentioned above, this is shown in Figure 3 together with the corresponding LIS. The same procedure was followed for the proton Fd model reported by Luo et al. (2017). As illustrated in this figure, a notable feature of the modulated electron spectrum is that the spectral slope changes around 100 MeV, but below this energy, the spectrum at the Earth and elsewhere in the heliosphere is essentially parallel with the LIS. This means that the total amount of modulation between the LIS and the spectrum at Earth is effectively constant at these low energies. As Moraal & Potgieter (1982) pointed out, this is due to the fact that electrons are relativistic and free to diffuse even at low energy, so that the spectral shape is dependent on the rigidity dependence of the diffusion coefficients. See also the reviews by Potgieter (2014b, 2017).

3.1. Fd Simulation without Drifts

To illustrate how diffusion, in particular, the rigidity dependence of the diffusion coefficients, affect a Fd profile, we manually switch off the drift term in the numerical simulation.

In Figure 4, panel (A) shows the simulated Fd profiles for 1 GV, 100 MV and 60 MV electrons. It demonstrates that for 60 MV and 100 MV electrons, the Fd profiles are nearly identical. As the rigidity increases, the magnitude of the Fd becomes much smaller: for the 1 GV case, the magnitude is around 15%, while the magnitude is around 50% for 100 MV and 60 MV electrons. Because CR electrons remain relativistic even at the low-rigidity level of 60 MV, they experience relatively little adiabatic energy losses (Potgieter 1996), so that diffusion dominates the transport process. Based on our assumptions, the value of the electron diffusion coefficient at 100 MV is the same as at 60 MV, while it is much larger for electrons around 1 GV; see Figure 1.

It is useful to note that Chih & Lee (1986) solved the diffusion-convection transport equation to find an analytical form for the Fd magnitude, which is written in terms of the change (decrease) in the CR intensity as

$$\frac{j_0 - j_m}{j_0} = \frac{V_{\rm sw}\left(\frac{\Delta K}{K}\right)L}{K}, \quad (18)$$

where j_0 is the undisturbed CR intensity and j_m is the minimum value in the Fd event; accordingly, the magnitude M is defined as $(j_0-j_m)/j_0$; K the diffusion coefficient in 1D, ΔK the change in the value of this diffusion coefficient inside the disturbance and L is the spatial extent of the disturbance (barrier) causing the Fd. According to Equation (18), the Fd magnitude is inversely proportional to K^2, so that a larger diffusion coefficient causes much smaller Fd's. It appears that the electron non-drift Fd simulation agrees rather well with this diffusion-convection regime.

In panel (B), the simulated Fd profiles for 1 GV, 100 MV, and 60 MV protons are illustrated. As the rigidity decreases, the Fd magnitude increases correspondingly: the magnitude is around 20% for 1 GV, 35% for 100 MV, and 85% for 60 MV. Concerning the value of diffusion coefficients, both the parallel and perpendicular diffusion coefficients increase as proton rigidity increases (see Figure 1). Thus, the overall trend is still consistent with the diffusion-convection scenario. In fact, based on PAMELA observations, Munini et al. (2018) recently demonstrated that a lower rigidity level corresponds to a larger Fd magnitude.

In panel (C), an electron Fd is compared to a proton Fd for the 1 GV case. As shown in Figure 1, the MFP for protons and electrons are almost the same at this rigidity. However, electrons at 1 GV is relativistic with $\beta \cong 1$, while 1 GV protons has a $\beta = 0.725$. Correspondingly, the diffusion coefficient value for 1 GV electrons is larger than for 1 GV protons, causing a somewhat smaller Fd magnitude; the 1 GV proton Fd profile has a larger magnitude comparing to the

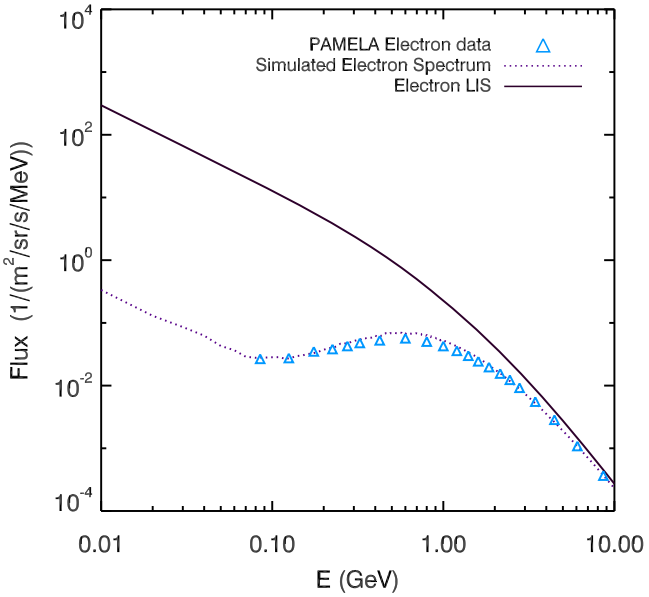

Figure 3. Computed, modulated electron spectrum at the Earth with respect to the electron LIS. This is compared with electron observations as measured by PAMELA in 2009 (Adriani et al. 2015).

simulated electron Fd profiles. In addition, the effect of adiabatic energy loss is more pronounced for 1 GV protons than for 1 GV electrons, causing some additional differences for the two Fd's. Similar to Panel (C), Panel (D) demonstrates the computed Fd profiles for 100 MV electrons and protons. For the protons $\beta = 0.1$, while for the electrons $\beta \cong 1$, so that the difference between electron and proton diffusion coefficient values becomes even larger than the 1 GV case. Correspondingly, the simulated Fd magnitude difference between 100 MV electrons and protons is significantly larger than the 1 GV case.

3.2. Drift Effects

In the following section, the simulation results are obtained by turning on the drift term when the transport Equation (1) is solved.

3.2.1. Drift Effects on Electron Fds

It is well known that the particle drifts play an important role in the global transport of CRs in the heliosphere (Jokipii et al. 1977; Kóta & Jokipii 1983; Potgieter & Moraal 1985; le Roux & Potgieter 1991). As the drift velocity of CR particles changes direction during a solar magnetic polarity reversal, two polarity epochs exist that affect CR depending on their charge sign; see also the reviews by Potgieter (2013, 2014a). Studying Fds during these polarity epochs provides another opportunity for clarifying these drift effects on CR modulation. Following previous reports (Lockwood & Webber 1986; le Roux & Potgieter 1991; Luo et al. 2017), the recovery time τ of a Fd is obtained by fitting the recovery phase with the following function:

$$j(t) = j_0 - (j_0 - j_m)e^{-(t-t_m)/\tau}, \quad (19)$$

where, as before, j_0 is the undisturbed cosmic ray intensity and t_m is the time when the cosmic ray intensity reaches the minimum value j_m in the Fd event.

Figure 5 demonstrates the features of the simulated Fd profiles for 1 GV and 100 MV electrons, respectively, for the two drift epochs, compared with the corresponding non-drift cases. Table 1 shows the computed recovery time and magnitude for the electron Fd profiles displayed in Figure 5. For the 1 GV case when the solar magnetic field is pointing inward in the northern heliosphere ($A < 0$ epoch), the recovery time is the shortest. For the non-drift case, the Fd recovers somewhat slower than the $A < 0$ case, but faster than the $A > 0$ case. According to drift theory, electrons drift inward toward Earth from the heliospheric polar regions down onto the equatorial plane and then outward along the equatorial HCS during $A < 0$ epochs. Consequently, apart from diffusion, the cavity behind the propagating disturbance (or barrier) is additionally filled with these electrons drifting from the polar regions so that the Fd recover faster than the non-drift case. Note that in a 3D case, particles also drift in the azimuthal direction, filling the cavity somewhat quicker than in the 2D case; see Luo et al. (2017). On the other hand, when electrons drift away from the equatorial plane during an $A > 0$ epoch, the recovery rate is less efficient than for the non-drift case. Overall, the interplay between the two diffusion processes and drift causes this difference in the recovery time. For the 100 MV electrons, in contrast, the recovery times for different cases is nearly the same. It is inferred that drift is now almost negligible because diffusion dominates the transport process for these low-rigidity electrons. In fact, as the transport process is mainly determined by diffusion for these low-rigidity electrons (Potgieter 1996), it has been widely used as a probe to study the diffusion coefficients and even magnetic turbulence (Zhang et al. 2007).

Concerning the magnitude of the Fd for these scenarios, the 1 GV electrons are very little influenced by changing the IMF polarity (switching drift directions), with only about a 5% difference between these scenarios. However, at 100 MV the magnitude is significantly larger than for the 1 GV case, consistent with the explanation given above that when the diffusion coefficients are much smaller the Fd magnitude increases accordingly.

3.2.2. Comparison of Proton and Electron Fds

Another method used to study drift effects is the analysis of Fd profiles for oppositely charged CR particles, since the drift motion is charge-dependent. In this section, this aspect is investigated for electron and proton Fds of the same rigidity. Figure 6 illustrated the simulated Fd profiles for 1 GV electrons and protons for the two solar magnetic polarity epochs. The magnitude and recovery time is demonstrated on Table 2. Evidently, while the magnitude varies little, the recovery times differ significantly. During the $A > 0$ epoch, the 1 GV proton Fd recovery time is remarkably shorter than the 1 GV electrons. On the other hand, the electrons display a faster recovery during the $A < 0$ epoch. Similar to our discussion above, this is interpreted as being consistent with the charge-sign dependent drift pattern: during $A > 0$ epoch, protons drift into the inner heliosphere from the polar regions, while electrons drift away from the equatorial plane. Because the cavity created behind the propagating disturbance (as CR barrier) is confined with a limited latitudinal (and longitudinal) extent away from the equatorial plane, the CR filling is more efficient for protons during an $A > 0$ epoch. The situation changes during an $A < 0$ epoch when electrons drift in from the polar regions and drift provides additional recovery so that the electron Fd recovers faster. In fact, this prediction of a charge-sign dependence for

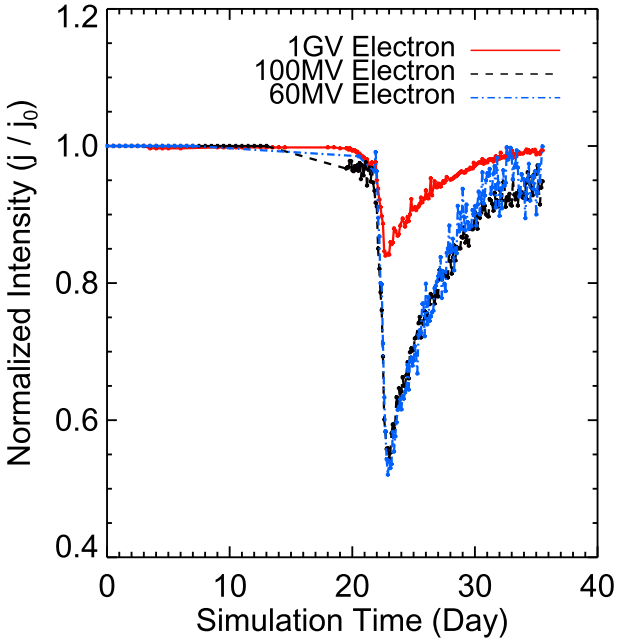

Panel A: Fd profiles for 1 GV, 100 MV and 60 MV electrons.

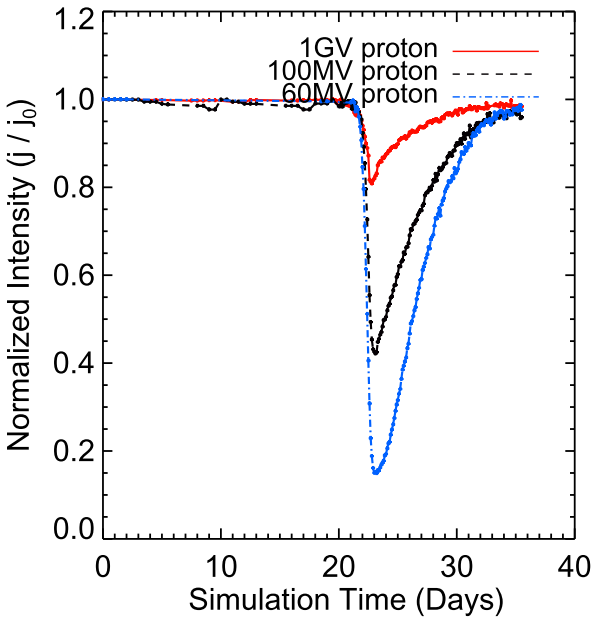

Panel B: Fd profiles for 1 GV, 100 MV and 60 MV protons.

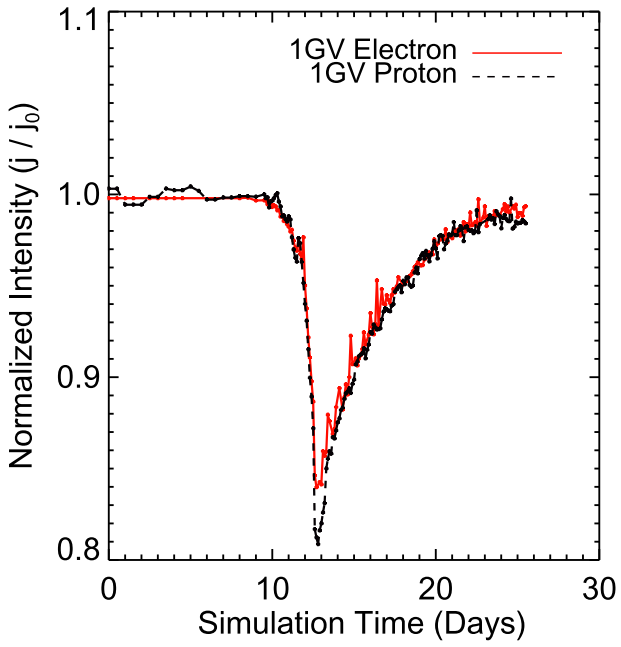

Panel C: Fd profiles, comparison between 1 GV electrons and protons.

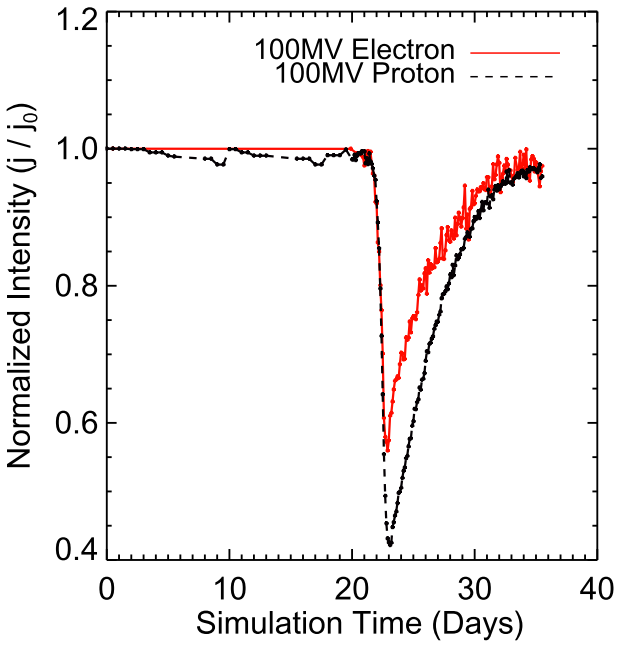

Panel D: Fd profiles, comparison between 100 MV electrons and protons.

Figure 4. Simulated Fd profiles for electrons and protons with different rigidity levels without drifts,. Panel A: the simulated Fd profiles for electrons with a rigidity of 1 GV, 100 MV and 60 MV. Panel B: the simulated Fd profiles for protons with rigidity of 1 GV, 100 MV, and 60 MV. Panel C: simulated Fd profiles for 1 GV electrons and protons. Panel D: simulated Fd profiles for 100 MV electrons and protons.

the Fd recovery times has just been reported for the first time by the PAMELA group (Munini et al. 2018). According to their report, the electron Fd indeed displays a faster recovery for the 2006 December Fd event when $A < 0$. As for the Fd magnitude, the drift term does not give any significant difference between electrons and protons (the overall difference is within 10%).

In Figure 7, the 100 MV electron and proton Fd profiles are presented; left (right) panel shows the $A > 0$ ($A < 0$) case. Table 3 illustrates the corresponding magnitude and recovery

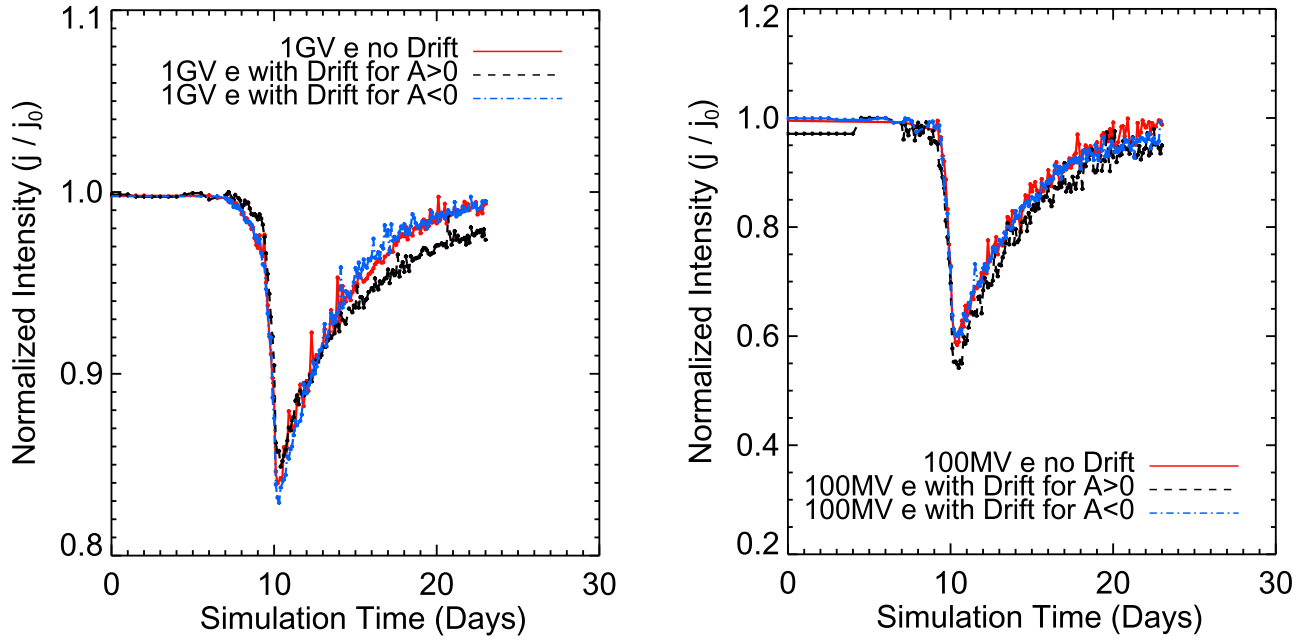

Figure 5. Simulated Fd profiles for 1 GV (left panel) and 100 MV (right panel) electrons for the two drift cycles, called $A < 0$ and $A > 0$, in comparison with the non-drift case.

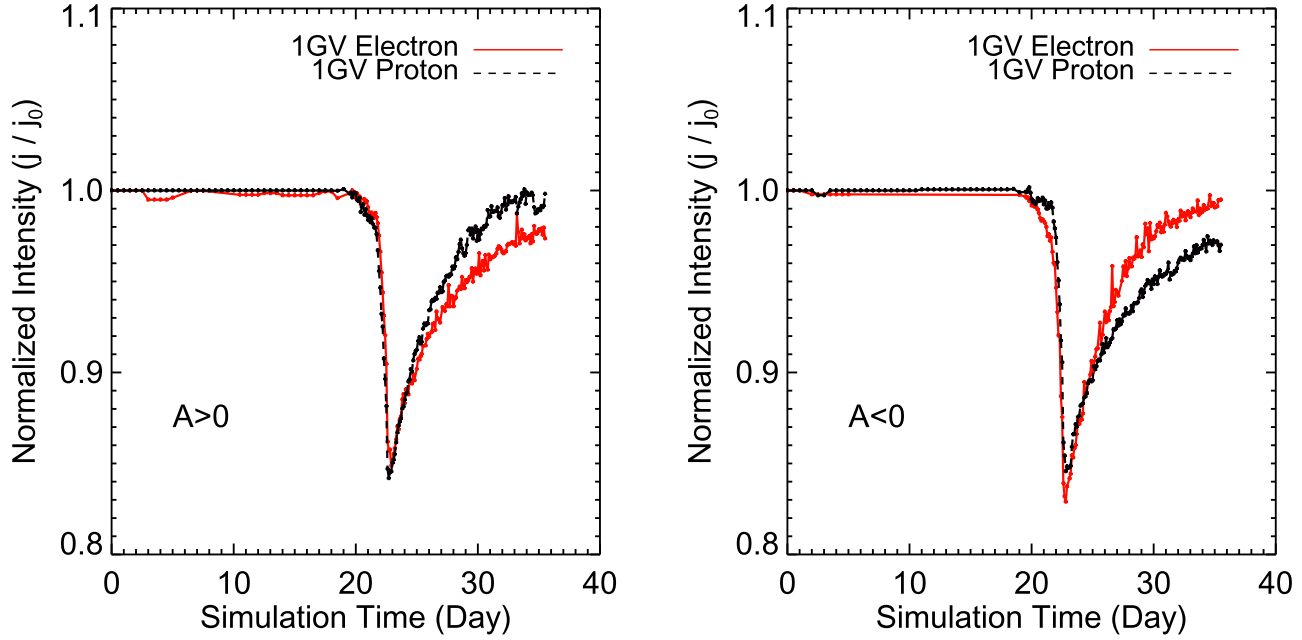

Figure 6. Simulated Fd profiles for electrons and protons with the same rigidity, at 1 GV. Left panel displays the $A > 0$ drift cycle, whereas the right panel displays the $A < 0$ cycle.

Table 1
Magnitude and Recovery Time for the Simulated Electron Fd Profiles Displayed in Figure 5

Parameter Values	Magnitude	Recovery Time (days)
1 GV non-drift	0.16	4.19
1 GV with drift for $A < 0$	0.17	3.67
1 GV with drift for $A > 0$	0.15	5.53
100 MV non-drift	0.43	4.71
100 MV with drift for $A < 0$	0.41	4.70
100 MV with drift for $A > 0$	0.45	4.76

time computed according Equation (19). During the $A > 0$ epoch, the proton Fd profile displays a somewhat faster recovery, following the trend in the 1 GV case shown in Figure 6. However, during the $A < 0$ epoch, the proton profile exhibits a similar recovery time than the electron profile. As previously argued, particle drift plays a lesser role for these low-rigidity electrons because diffusion is the dominating process. Consequently, the electron recovery time is almost the same for both $A > 0$ and $A < 0$ epochs, as the simulation results illustrate. The 100 MV proton Fd is still been affected by drift, thus it exhibits a polarity dependence and the Fd recovers faster during the $A > 0$ epoch. Because the diffusion

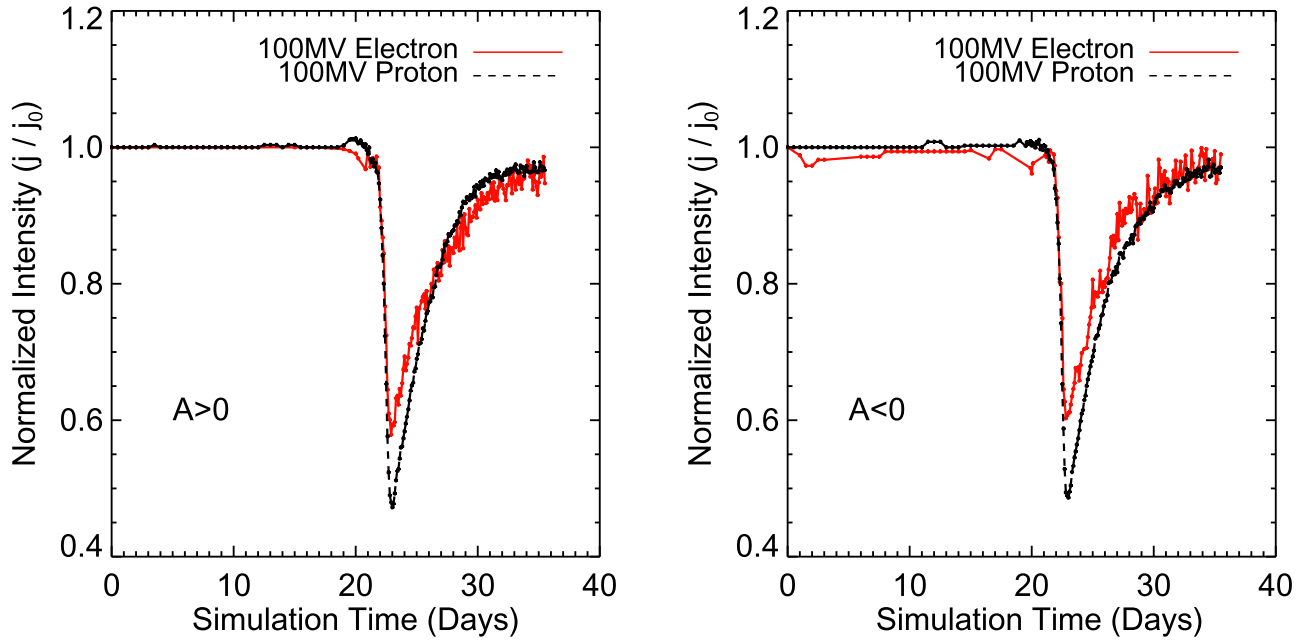

Figure 7. Simulated Fd profiles for electrons and protons at 100 MV. Left panel displays the $A > 0$ drift cycle, whereas the right panel displays the $A < 0$ cycle.

Table 2
The Magnitude and Recovery Time for the Simulated Electron Fd Profiles as Displayed in Figure 6

Parameter Values	Magnitude	Recovery Time (days)
1 GV Electron $A > 0$	0.15	5.53
1 GV Proton $A > 0$	0.16	3.75
1 GV Electron $A < 0$	0.17	3.67
1 GV Proton $A < 0$	0.15	6.17

Table 3
The Magnitude and Recovery Time for the Simulated Electron Fd Profiles as Displayed in Figure 7

Parameter Values	Magnitude	Recovery Time (days)
100 MV Electron $A > 0$	0.420	4.57
100 MV Proton $A > 0$	0.527	3.49
100 MV Electron $A < 0$	0.413	4.63
100 MV Proton $A < 0$	0.516	4.56

coefficients for 100 MV protons is smaller than for 100 MV electrons, the proton Fd profile exhibits a larger magnitude for both $A > 0$ and $A < 0$ epochs.

The simulation results suggest that the Fd magnitude is mainly determined by the diffusion process. According to le Roux & Potgieter (1991), a general and useful rule is that the magnitude of the Fd is determined by the local modulation conditions where the disturbance is located in the heliosphere, whereas the recovery time is much more influenced by the conditions that the propagating disturbance encounters and the global conditions that prevails while the Fd is propagating outward; see also the discussion by Luo et al. (2017).

4. Discussion and Conclusions

The full time-dependent, 3D Parker transport equation is solved using the SDE method to simulate electron Fds, similar to our previous report on proton Fds, utilizing the simplified concept of a propagating CR barrier. As far as we know, this is the first attempt to study electron Fds in a full 3D numerical model. A new LIS for Galactic electrons is applied. The model is first validated by reproducing the 2009 electron spectrum observed at the Earth by PAMELA. As such, the numerical procedure settles on a set of diffusion coefficients; a drift coefficient and relevant modulation parameters such as the solar wind and IMF; and the position of the outer modulation boundary.

Electron Fd profiles are simulated for various rigidity levels, for both non-drift cases and for maximum drifts during the two known drift cycles to establish to what extent gradient and curvature drifts as a global modulation process, influences the profile of a typical electron Fd. This is then compared with proton Fd to investigate the charge-sign dependence related to Fds.

The simulation has revealed that the magnitude of Fds remains essentially unchanged for low-rigidity electrons, e.g., the 100 MV Fd magnitude is the same as the 60 MV Fd magnitude. This is because CR electrons remain relativistic to these low values and that the diffusion coefficients remain as such essentially unchanged to become the dominating modulation process. Adiabatic energy loss for these electrons is small, in contrast to the case for protons where adiabatic energy loss determines the shape of proton spectra at Earth at these low rigidities. Interesting is that in this context, our 3D numerical results become surprisingly consistent with a diffusion-convection scenario used by Chih & Lee (1986). It follows that at these low rigidities, drift effects on electron Fd's insignificant but become more evident with increasing rigidity as shown in Figure 4. For proton Fd's, drift effects remain present, although small, down to the lowest rigidities. See also the discussion by Potgieter (2017).

Our results are summarized in Tables 2 and 3. It follows that during the $A > 0$ epoch, the 1 GV proton Fd recovery time is remarkably shorter than the 1 GV electrons, whereas the electron

Fd display a faster recovery during the $A < 0$ epoch, in line with what one expects from a drift point of view. However, as for the Fd magnitude, drifts do not give a significant difference between electrons and protons (the overall difference is within 10%). Our simulation results suggest that the Fd magnitude is mainly determined by the diffusion process, in particular, the local modulation conditions where the disturbance is located in the heliosphere, whereas the recovery time is much influenced by the conditions that the propagating disturbance encounters and the global conditions that prevails while the Fd is propagating outward toward the HP.

Most encouraging is that for the first time, the precise PAMELA observations allowed the study of the behavior of different particle species during a Fd. In particular, protons, helium nuclei, and electrons were compared. The proton and the helium nuclei Fd amplitude and the recovery time were reported to be in good agreement, while electrons showed, on average, a faster recovery time, which tended to approach the proton recovery time as the rigidity increased. They interpret this behavior as a charge-sign dependence caused by the different global drift pattern between protons and electrons. A next step is to study the behavior of what they reported with the predictions of this model. This will be the topic of a future report. As the AMS02 experiment provides accurate electron fluxes, Fd profiles for different rigidity electrons should also be obtained (Bindi et al. 2017). Correspondingly, the relationship between the Fd magnitude and its rigidity can be studied in detail using the experimental data and numerical modeling. Utilizing the mentioned "diffusion-regime" feature, studying observed electron Fd profiles may shed light on the rigidity dependence of the related diffusion coefficients. Evidently, if proton and electron Fd's can be observed with almost the same accuracy, drifts effects on transient phenomena can be investigated in detail, escpecially with increasing solar activity.

The work is jointly supported by the National Natural Science Foundation of China (41774185, U1738128, 41731067, and 41531073) and the Specialized Research Fund for State Key Laboratories. Xi Luo acknowledges the support of the post-doctoral program of the North-West University in South Africa. M.S.P. acknowledges the financial support of the South African National Research Foundation (NRF) under the Competitive Funding for Rated Researchers, grant 68198. M.Z. was supported in part by NASA Grants NNX14AJ53G and NNX15AN72G. This material is based upon work supported by the US National Science Foundation under grant No. CNS 09-23050.

ORCID iDs

Xi Luo https://orcid.org/0000-0002-4508-6042
Marius S. Potgieter https://orcid.org/0000-0001-8615-1683
Ming Zhang https://orcid.org/0000-0003-3529-8743
Xueshang Feng https://orcid.org/0000-0001-8605-2159

References

Adriani, O., Barbarino, G. C., Bazilevskaya, G. A., et al. 2013, ApJ, 765, 91
Adriani, O., Barbarino, G. C., Bazilevskaya, G. A., et al. 2015, ApJ, 810, 142
Bieber, J. W., Matthaeus, W. H., Smith, C. W., et al. 1994, ApJ, 420, 294
Bindi, V., Corti, C., Consolandi, C., et al. 2017, AdSpR, 60, 865
Bisschoff, D., & Potgieter, M. S. 2014, ApJ, 794, 166
Bisschoff, D., & Potgieter, M. S. 2016, Ap&SS, 361, 48
Cane, H. V. 2000, SSRv, 93, 55
Chih, P. P., & Lee, M. A. 1986, JGR, 91, 2903
Corti, C., Bindi, V., Consolandi, C., & Whitman, K. 2016, ApJ, 829, 8
Forbush, S. E. 1937, PhRvL, 51, 1108
Gurnett, D. A., Kurth, W. S., Burlaga, L. F., & Ness, N. F. 2013, Sci, 341, 1489
Herbst, K., Muscheler, R., & Heber, B. 2017, JGR, 122, 23
Jokipii, J. R., & Barry, T. 1981, ApJ, 243, 1115
Jokipii, J. R., Levy, E. H., & Hubbard, W. B. 1977, ApJ, 213, 861
Kadokura, A., & Nishida, A. 1986, JGR, 91, A1
Kopp, A., Büsching, I., Strauss, R. D., & Potgieter, M. S. 2012, CoPhC, 183, 530
Kóta, J., & Jokipii, J. R. 1983, ApJ, 265, 573
le Roux, J. A., & Potgieter, M. S. 1991, A&A, 243, 531
Lockwood, J. A., & Webber, W. R. 1986, JGR, 91, 2851
Luo, X., Potgieter, M. S., Zhang, M., et al. 2016, ApJ, 826, 182
Luo, X., Potgieter, M. S., Zhang, M., & Feng, X. 2017, ApJ, 839, 53
Luo, X., Zhang, M., Feng, X., & Mendoza-Torres, J. E. 2013, JGR, 118, 7517
Luo, X., Zhang, M., Rassoul, K. H., & Pogorelov, N. V. 2011, ApJ, 730, 13
Martucci, M., Munini, R., Boezio, M., et al. 2018, ApJL, 854, L2
Meyer, P., & Simpson, J. R. 1955, PhRv, 99, 1517
Meyer, P., & Simpson, J. R. 1957, PhRv, 106, 568
Moraal, H., & Potgieter, M. S. 1982, Ap&SS, 84, 519
Morrison, P. 1956, PhRv, 101, 1397
Munini, R., Boezio, M., Bruno, A., et al. 2018, ApJ, 853, 76
Ngobeni, D. M., & Potgieter, M. S. 2015, AdSpR, 56, 1525
Parker, E. N. 1965, P&SS, 13, 9
Potgieter, M. S. 1996, JGR, 101, 24411
Potgieter, M. S. 2013, LRSP, 10, 3
Potgieter, M. S. 2014a, AdSpR, 53, 1415
Potgieter, M. S. 2014b, BrJPh, 44, 581
Potgieter, M. S. 2017, AdSpR, 60, 848
Potgieter, M. S., & Moraal, H. 1985, ApJ, 294, 425
Potgieter, M. S., & Nndanganeni, R. R. 2013, APh, 48, 25
Potgieter, M. S., Vos, E. E., Munini, R., Boezio, M., & Felice, V. Di. 2015, ApJ, 810, 141
Qin, G., Zhang, M., & Dwyer, J. R. 2006, JGR, 111, A08101
Simpson, J. A. 1953, Univ. Chicago Mag., 45, 5
Teufel, A., & Schlickeiser, R. 2003, A&A, 397, 15
Vos, E. E., & Potgieter, M. S. 2015, ApJ, 815, 119
Webber, W. R., & McDonald, F. B. 2015, GeoRL, 40, 1665
Zhang, G., & Burlaga, L. F. 1988, JGR, 93, 2511
Zhang, M. 1999, ApJ, 513, 409
Zhang, M., Luo, X., & Pogorelov, N. 2015, PhPl, 22, 091501
Zhang, M., Qin, G., Rassoul, H., et al. 2007, P&SS, 55, 12
Zhao, L. L., Qin, G., Zhang, M., & Heber, B. 2014, JGR, 119, 1493